

Influence of Midlatitude Winds on the Stratification of the Equatorial Thermocline*

MASAMI NONAKA

Frontier Research Center for Global Change, Japan Agency for Marine-Earth Science and Technology, Yokohama, Japan

JULIAN P. MCCREARY JR.

International Pacific Research Center, and Department of Oceanography, University of Hawaii at Manoa, Honolulu, Hawaii

SHANG-PING XIE

International Pacific Research Center, and Department of Meteorology, University of Hawaii at Manoa, Honolulu, Hawaii

(Manuscript received 12 November 2004, in final form 14 July 2005)

ABSTRACT

The stratification of the equatorial thermocline is a key variable for tropical climate dynamics, through its influence on the temperature of the water that upwells in the eastern equatorial ocean. In this study, two types of ocean models are used, an ocean general circulation model (GCM) and a 1½-layer model, to investigate processes by which changes in the midlatitude winds affect the equatorial stratification. Specifically, the influences of anomalous mode-water formation, Ekman pumping, and entrainment in the subpolar ocean are examined. The effects of a “sponge layer” adjacent to the northern boundary of the basin are also assessed. Solutions are forced by idealized zonal winds with strong or weak midlatitude westerlies, and they are found in rectangular basins that extend from the equator to 36°N (small basin) or to 60°N (large basin). In the GCM solutions, a prominent response to reduced winds is the thinning of the mixed layer in the northwestern region of the subtropical gyre, leading to less subduction of low-potential-vorticity mode water and hence thinning of the upper thermocline in the central-to-eastern subtropics. Almost all of this thinning signal, however, recirculates within the subtropics, and does not extend to the equator. Another midlatitude response is shallowing (deepening) of the thermocline in the subtropical (subpolar) ocean in response to Ekman pumping. This, primarily, first-baroclinic-mode ($n = 1$) response has the most influence on the equatorial thermocline. First-baroclinic-mode Rossby waves propagate to the western boundary of the basin where they reflect as packets of coastal Kelvin and short-wavelength Rossby waves that carry the midlatitude signal to the equator. Subsequently, equatorial Kelvin waves spread it along the equator, leading to a shoaling and thinning of the equatorial thermocline. The layer-thickness field h in the 1½-layer model corresponds to thermocline depth in the GCM. Both the sponge layer and subpolar Ekman suction are important factors for the 1½-layer model solutions, requiring water upwelled in the interior ocean to be transported into the sponge layer via the western boundary layer. In the small basin, equatorial h thins in response to weakened westerlies when there is a sponge layer, but it *thickens* when there is not. In the large basin, equatorial h is unaffected by weakened westerlies when there is a sponge layer, but it thins when water is allowed to entrain into the layer in the subpolar gyre. It is concluded that the thinning of the equatorial thermocline in the GCM solutions is caused by the sponge layer in the small basin and by entrainment in the subpolar ocean in the large one.

1. Introduction

The stratification of the equatorial thermocline is believed to be a key variable for global climate, poten-

tially affecting the intensity, period, and other properties of the El Niño–Southern Oscillation (ENSO) through its influence on the temperature of the water that upwells in the eastern Pacific (Fedorov and Philander 2000; An and Jin 2000). The factors that control the equatorial stratification, however, are currently not well understood.

Recent studies show that the equatorial thermocline is connected to the subtropics by a pair of shallow overturning cells on either side of the equator, called the subtropical cells (STCs) (McCreary and Lu 1994; Pedlosky 1996). Because of this connection, the STCs have been hypothesized to play a role in equatorial tempera-

*International Pacific Research Center Contribution Number 360 and School of Ocean and Earth Science and Technology Contribution Number 6700.

Corresponding author address: Dr. Masami Nonaka, Frontier Research Center for Global Change, Japan Agency for Marine-Earth Science and Technology (JAMSTEC), 3173-25 Showa-machi, Kanazawa-ku, Yokohama 236-0001, Japan.
E-mail: nona@jamstec.go.jp

ture variability through either of the following mechanisms: (i) advection to the equator of temperature anomalies formed by subtropical subduction (Gu and Philander 1997) or (ii) changes in STC strength, which cause equatorial sea surface temperature anomalies (SSTAs) by varying the amount of the cold water that is transported into the Tropics (Kleeman et al. 1999; Nonaka et al. 2002; Solomon et al. 2003).

Liu and Philander (1995) reported a solution to an idealized ocean general circulation model (GCM) in which weakened midlatitude westerlies strengthened the equatorial stratification. They speculated that, under stronger westerly winds, the resulting deeper subtropical thermocline allows the STCs to advect warmer water to the equator, deepening the thermocline there as well. If proven true, their solution illustrates another mechanism for causing equatorial temperature variability, different from those of Gu and Philander (1997) and Kleeman et al. (1999): It is similar to the former study in that surface temperature anomalies subducted in the subtropics are advected to the equator, but the temperature anomalies are wind driven rather than determined by an externally specified heat flux; it differs from the latter study in that their midlatitude wind anomalies have little effect on STC strength (Liu and Philander 1995; Klingner et al. 2002).

The present study investigates how changes in midlatitude winds influence thermocline structure both at midlatitudes and near the equator, contrasting solutions to ocean models forced by idealized wind fields with stronger and weaker midlatitude westerlies. We use two types of ocean models: an oceanic GCM and a 1½-layer model. The latter model is useful for understanding basic adjustment dynamics at work in the GCM, as its layer-thickness field corresponds to the depth and thickness of the GCM's thermocline.

As we shall see, weakened westerlies alter the midlatitude thermocline structure in two ways: by thinning the mixed layer, thereby weakening mode-water formation, and by anomalous Ekman pumping. The former process does not much affect the equatorial thermocline, as most of the mode water recirculates in the subtropical gyre, but the latter one does. The influences of a "sponge layer" adjacent to the northern boundary of the basin and of entrainment in the subpolar ocean ultimately determine the equatorial response. Indeed, the behavior of the Liu and Philander (1995) solutions noted above is traceable to the sponge layer in their model.

The paper is organized as follows. Section 2 describes the model and experiments. Section 3 discusses solutions to the GCM, considering effects due to mixed layer processes and to Ekman pumping. Section 4 re-

ports solutions to the 1½-layer model, separating wind-driven effects from those caused by the sponge layer and entrainment. Section 5 provides a summary and discussion.

2. Models and experiments

a. GCM

The ocean GCM is based on Geophysical Fluid Dynamics Laboratory (GFDL) Modular Ocean Model (MOM 1.1) (Pacanowski et al. 1991), with salinity fixed at 35 psu. The model solves the primitive equations in spherical coordinates under the Boussinesq, rigid-lid, and hydrostatic approximations. The horizontal eddy viscosity and diffusivity are assumed constant with $\nu_h = 2.0 \times 10^7 \text{ cm}^2 \text{ s}^{-1}$ and $\kappa_h = 1.0 \times 10^7 \text{ cm}^2 \text{ s}^{-1}$, respectively. The vertical mixing coefficients depend on the Richardson number (Pacanowski and Philander 1981) with a background diffusivity and viscosity of 0.1 and $1.0 \text{ cm}^2 \text{ s}^{-1}$, respectively.

The model basin is rectangular, extending from the equator to either $y_n = 36^\circ\text{N}$ or 60°N , with a width $L = 60^\circ$ and a constant depth of 5000 m. The zonal resolution of the grid is 1° , and its meridional resolution varies gradually from 1° at midlatitudes to $\frac{1}{3}^\circ$ at the equator. There are 41 levels in the vertical with a resolution of 10–15 m in the upper 300 m. The model employs no-slip conditions on the northern, eastern, and western boundaries, symmetric conditions on the equator, and requires that the temperature flux vanishes on all boundaries. Because allowing for salinity variations is not essential in our process-oriented study, salinity is kept fixed at 35 psu. The initial temperature state (Fig. 1, middle panel) is determined from the zonal average of the annual-mean density field in the North Pacific Ocean. Model sea surface temperature (SST) is relaxed to $T^*(x)$, the initial state adjusted to a constant value south of 6.5°N (Fig. 1, solid curve in top panel), with a restoring time of 50 days for a water column of 10 m.

Within 5° of the northern boundary there is a "sponge layer" in which temperature is relaxed to its initial state throughout the water column with a restoring time that monotonically increases from 2 to 900 days at grid points 0.5° – 4.5° from the boundaries. In the large basin, we interpret the sponge layer to represent the effect of strong thermodynamic processes (e.g., deep convection) external to the basin. In the small basin, the relaxation to zonally uniform temperature field is problematic since winds near the boundary drive a significant meridional geostrophic current there.

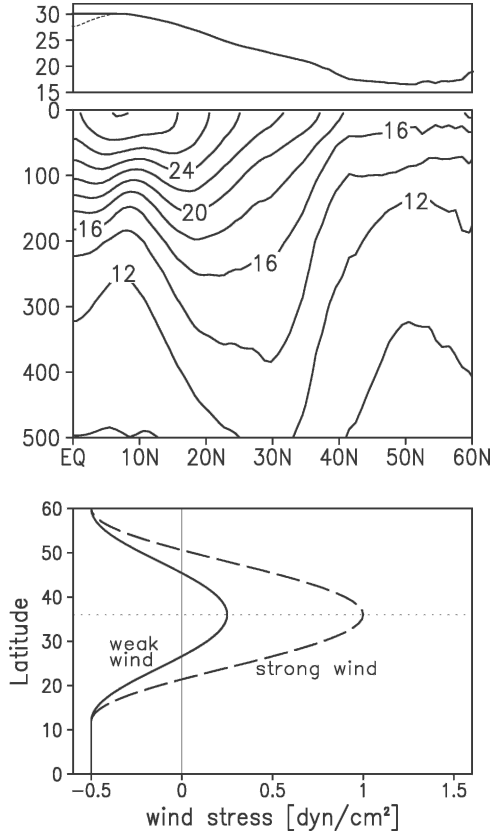


FIG. 1. (top) Meridional profiles for the initial SST field (dashed line) and T^* (solid line), the temperature to which model SST is restored. (middle) Latitude–depth section of the initial temperature field. In the sponge layer near the northern boundary, temperature is restored to this field. Contour intervals are 2°C . (bottom) Meridional structure of the zonal wind stress (dyn cm^{-2}) that forces solutions S and L (dashed line) and solutions SR and LR (solid line). Wind stress curl for the weak winds is one-half times that for the strong winds.

b. The $1\frac{1}{2}$ -layer model

Equations for the numerical $1\frac{1}{2}$ -layer model are

$$\begin{aligned} u_t - fv + g'h_x &= \frac{\tau^x(y)}{\rho_1 H} + \nu_h \nabla^2 u - \alpha u, \\ v_t + fu + g'h_y &= + \nu_h \nabla^2 v - \alpha v, \quad \text{and} \\ h_t &= H(u_x + v_y) + w_1 + w_s, \end{aligned} \quad (1)$$

where H is the background layer thickness, g' is a reduced-gravity coefficient, and τ^x is defined in (9) below. Entrainment into the layer,

$$w_1 = \frac{h - H'}{t_1} \theta(H' - h), \quad (2)$$

is also allowed, where θ is a step function and $t_1 = 10^5$ s. According to (2), entrainment occurs whenever h be-

comes thinner than H' so that H' simulates the depth of a surface mixed layer. The coefficients for Rayleigh friction and Laplacian mixing are given by

$$\alpha = \alpha_0 \theta(\delta x - x) \quad \text{and} \quad \nu_h = \nu_{h0} \theta(x - \delta x), \quad (3)$$

where $\delta x = 3^\circ$; thus, Laplacian mixing is active over most of the interior ocean, switching to Rayleigh friction only within 3° of the western boundary (at $x = 0$). (Without the switch to Rayleigh friction, h fields in numerical solutions to the $1\frac{1}{2}$ -layer model with entrainment were significantly thicker than their analytic counterparts. This discrepancy is traceable to the property that the Munk western boundary layer has an offshore countercurrent and, hence, an overshoot of h . In contrast, there is no overshoot in the western boundary layer due to Rayleigh friction.)

Unless specified otherwise, $g' = 6.0 \text{ cm s}^{-2}$, $\nu_{h0} = 5.0 \times 10^7 \text{ cm}^2 \text{ s}^{-1}$, $\alpha_0 = 1.0 \times 10^6 \text{ s}^{-1}$, $H = 150 \text{ m}$, $H' = 50 \text{ m}$, and $\rho_1 = 1.0 \text{ gm cm}^{-3}$ is the density of the layer. The stratification parameters, H and g' , correspond to the thickness and strength of the tropical thermocline, the value of $g' = \alpha g \Delta T$ representing a temperature jump across the layer of $\Delta T = 24^\circ\text{C}$ when $\alpha = 2.5 \times 10^{-4} \text{ }^\circ\text{C}^{-1}$ (Fig. 1). We note that the model's response depends on the product $g'H$ rather than each parameter separately (section 4). With the aforementioned choices, $\sqrt{g'H} = 300 \text{ cm s}^{-1}$, a reasonable value of the characteristic speed of the $n = 1$ mode.

The model basin and boundary conditions are the same as those used for the GCM. A sponge layer w_s can be included near the northern boundary, in which case

$$w_s = \frac{h - H}{t_r} \theta(y - y'_n), \quad (4)$$

where θ is a step function, $y'_n = y_n - \Delta y$, $\Delta y = 5^\circ$,

$$t_r = t_s 10^{-(y - y_n + 0.5)/\delta y}, \quad (5)$$

$t_s = 10^5$ s, and $\delta y = 1^\circ$. According to (4) and (5), h is relaxed back to H in the sponge layer with a damping time t_r that decreases by a power of 10 per degree away from the northern boundary. At $y = y_n - 0.5^\circ$, the location of the h point nearest the boundary, $t_r = t_s$.

Equations for the analytic version of the $1\frac{1}{2}$ -layer model are

$$\begin{aligned} -fv + g'h_x &= \frac{\tau^x(y)}{\rho_1 H}, \\ fu + g'h_y &= 0, \quad \text{and} \\ H(u_x + v_y) + w_1 + w_s &= 0. \end{aligned} \quad (6)$$

Horizontal mixing is not explicitly included in (6) but is presumed to be present in western and northern bound-

ary layers with ν_h small enough for the width of the boundary layers to be negligible. In this version, w_1 is (2) in the limit that $t_1 \rightarrow 0$, essentially replacing (2) by the constraint that

$$h \geq H'. \tag{7}$$

According to (7), in regions where $h = H'$ water instantly upwells into the layer in response to any divergence in the interior ocean driven by Ekman pumping. Similarly, velocity w_s is given by (4) in the limits that $\Delta y \rightarrow 0$ and $t_s \rightarrow 0$, yielding the constraint

$$h = H \quad \text{at} \quad y = y_n. \tag{8}$$

According to (8), the sponge layer instantly absorbs any divergence or convergence of the northern boundary current (NBC), upwelling or downwelling water from the layer as required.

c. Experimental design

The models are forced by an idealized, x -independent, zonal wind stress field of the form

$$\tau^x(y) = \begin{cases} \tau_o \theta(t), & y \leq y_1 \\ \left[\tau_o + \frac{1}{2} \Delta\tau \left(1 - \cos 2\pi \frac{y - y_1}{y_2 - y_1} \right) \right] \theta(t), & y_1 < y \leq y_2, \end{cases} \tag{9}$$

where $y_1 = 12^\circ\text{N}$, $y_2 = 60^\circ\text{N}$, and $\theta(t)$ is a step function. According to (9), τ^x consists of two parts: background winds τ_o corresponding to easterly winds in the Tropics and midlatitude westerlies proportional to $\Delta\tau$. In Fig. 1 (bottom) are plotted the two wind fields that force the numerical solutions, for which $\tau_o = -0.5 \text{ dyn cm}^{-2}$ and $\Delta\tau$ is either 1.5 dyn cm^{-2} (strong winds) or 0.75 dyn cm^{-2} (weak winds). They differ in the strength of their westerlies with midlatitude wind curl being 2 times as strong for one of them (dashed curve) as for the other (solid curve), and we refer to them below as “strong” and “weak” winds, respectively.

The numerical solutions forced by strong winds are almost all integrated from a state of rest for a period of 90 years, which for convenience we define to range from year -50 to year $+40$. Solutions forced by weak winds are almost all integrated for 40 years, using year 0 of the corresponding strong-wind solution as their initial state. In the following analyses, these solutions are compared in overlapping time periods from 0 to 40 years. Exceptions are for the $1\frac{1}{2}$ -layer solutions with entrainment, which are spun up for a period of 250 years beginning from their corresponding solution without entrainment [section 4b(2)]. In addition, a test so-

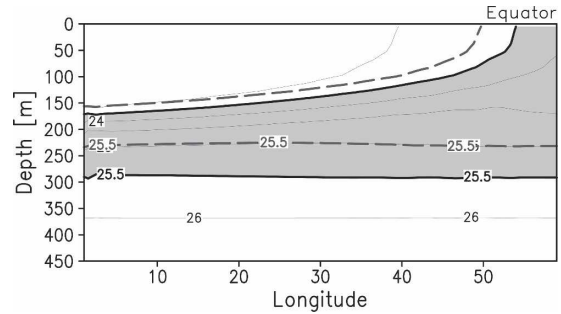


FIG. 2. Longitude–depth section of density fields at the equator in year 40. Solid contours with shading are for solution S and dashed contours are for solution SR. For solution S, density between 23.5 and $25.5 \sigma_\theta$ is shaded, and contour intervals are $0.5 \sigma_\theta$. For solution SR, contours for only 23.5 and $25.5 \sigma_\theta$ are plotted.

lution to the GCM is obtained forced by strong winds with solution LR at year 40 as its initial state (section 5).

3. Solutions to the GCM

In most of this section, we compare pycnocline structures for the GCM solutions obtained in the small basin (section 3a). First, we describe equatorial differences between the solutions forced by strong and weak winds [section 3a(1)]. Then, we discuss two prominent processes that cause midlatitude differences, namely, mixed layer processes [section 3a(2)] and Ekman pumping [section 3a(3)], finding that only the latter significantly impacts the equatorial stratification. Last, we report on solutions in the large basin (section 3b). For convenience, we refer to the GCM solutions forced by strong and reduced winds in the smaller basin ($y_n = 36^\circ\text{N}$) as “solution S” and “solution SR,” respectively, and in the larger basin ($y_n = 60^\circ\text{N}$) as “solution L” and “solution LR.” Solutions S and SR are equivalent to the Liu and Philander (1995) solutions referred to in the introduction.

a. Small basin

1) EQUATORIAL REGION

Figure 2 shows longitude–depth sections of equatorial density at year 40 for solutions S (solid) and SR (dashed). For each solution, the largest density gradient lies in the range 23.5 – $25.5 \sigma_\theta$ (both at the equator and midlatitudes), and we refer to this region as the model’s thermocline. Both the bottom ($25.5 \sigma_\theta$) and top ($23.5 \sigma_\theta$) of the equatorial thermocline in solution SR are shallower than they are in solution S. The change in bottom depth, however, is larger than that of the top, and thus the equatorial thermocline is *thinner* in SR, strengthening the stratification. Note also that the tilt of

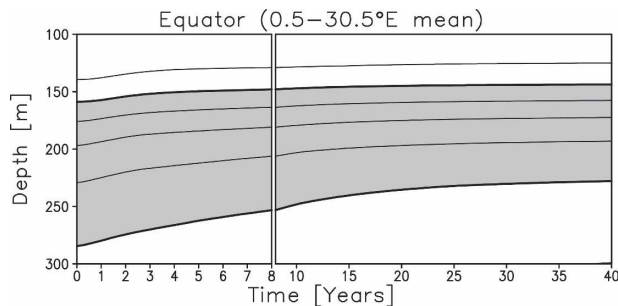


FIG. 3. Time-depth diagram of equatorial density for solution SR, averaged from the western boundary to 30°E. Contour intervals are $0.5 \sigma_{\theta}$, and densities between 23.5 and $25.5 \sigma_{\theta}$ are shaded.

the thermocline along the equator is little changed in SR, a consequence of the equatorial easterlies being unchanged in both solutions.

Figure 3 shows how the equatorial pycnocline develops with time in solution SR. It begins to shoal very soon after the wind anomaly is switched on, indicating the influence of midlatitude signals that quickly propagate to the equator along the western boundary. Individual isopycnals shallow monotonically in time, with

deeper ones tending to shoal more than upper ones. These properties indicate that the stratification change is largely induced by first-baroclinic-mode ($n = 1$) signals.

The strengths of the STCs in the two solutions are almost the same, consistent with previous studies that show STC strength to be determined mainly by the tropical easterlies with very little influence from the midlatitude westerlies (McCreary and Lu 1994; Liu and Philander 1995; Klinger et al. 2002). This property shows that the equatorial cooling in the subsurface layer in solution SR (Fig. 2) does not result from the Kleeman et al. (1999) mechanism. Additionally, reduced southward Ekman flow in solution SR warms SST in the subtropics (see the discussion of Fig. 4 next), indicating that the cooling is also not due to advection of subducted temperature anomalies as in the Gu and Philander (1997) mechanism.

2) MIXED LAYER PROCESSES

A striking change in the subtropics when the winds are weakened is a thinning of the mixed layer and its subsequent influence on midlatitude stratification. In

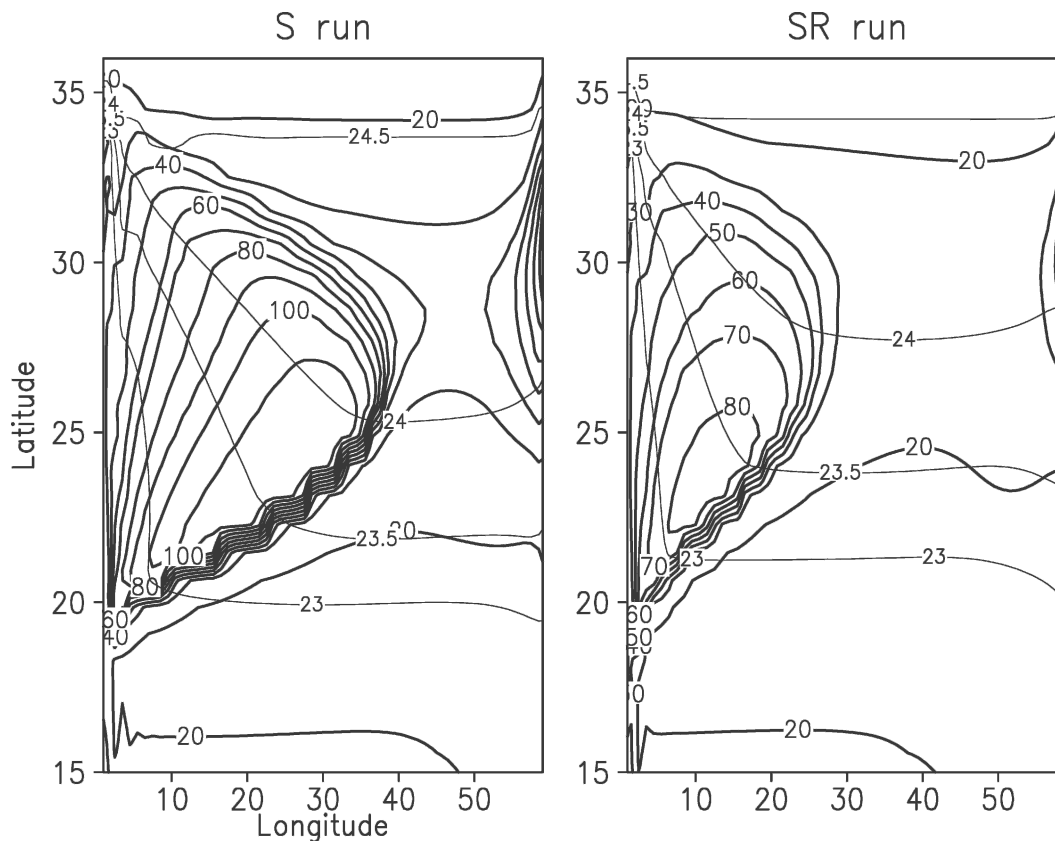


FIG. 4. Sea surface density (thin contours) and mixed layer depth (thick contours) in solutions (left) S and (right) SR in year 40. Contour intervals are $0.5 \sigma_{\theta}$ for density and 10 m for mixed layer depth.

Fig. 4 steady-state, mixed layer thickness (MLD) fields are plotted for solutions S (left) and SR (right), with MLD defined to be the depth where the density difference from the surface value is $0.05 \sigma_\theta$. In solution S, the MLD is thick in a wedge-shaped region in the western and central subtropics. One cause of this region is the poleward and eastward advection of warm tropical waters in the subtropical gyre; the resulting cooling of these waters by the surface heat flux enhances convective mixing and, hence, thickens the mixed layer. Another cause is equatorward Ekman drift that advects cooler surface water over warmer subsurface water, again intensifying convective mixing. In contrast, the mixed layer is thin in the southeastern subtropics where cool water advects southward within the subtropical gyre and is warmed at the surface, thereby reducing convection. As a result, along the southeastern edge of the thick mixed layer region, there is a strong MLD front (e.g., Nishikawa 2003). A similar MLD distribution is found in the real North Pacific (e.g., Qiu and Huang 1995). The MLD is much shallower in the central and western ocean in solution SR, a consequence of there being less poleward advection of warm water in a weakened western boundary current (WBC) and reduced southward Ekman transport in the surface layer.

The MLD front influences the density structure of subsurface waters through subduction, thereby setting the stratification of the upper thermocline in the subtropics. Mode waters [i.e., subsurface waters with a large thickness, q , and low potential vorticity (PV)] are generated by subduction whenever there is a flow across the intersection of the MLD front with a density outcrop line (Kubokawa 1999; Xie et al. 2000). In Fig. 5 density sections along 21°N are plotted, and the presence of mode waters in solution S (top panel) is apparent in the central to eastern ocean with regions of weakened stratification extending eastward and downward across most of the basin. Mode water with densities centered near $24.0 \sigma_\theta$, say, is found near 45°E at depths of 100–150 m; it was generated by subduction across the MLD front at $24.0 \sigma_\theta$ surface isopycnals (Fig. 4, left panel), and then carried southeastward within the circulation of the subtropical gyre. Deeper mode waters are found in more eastern areas because outcrop lines of denser surfaces cross the MLD front at more northeastern points (Fig. 4, left) and they must travel farther under the action of the downwelling-favorable Ekman pumping to reach 21°N . Because the MLD is thinner in solution SR, q is smaller for the subducted waters. Indeed, there is almost no high- q (low PV) mode water in the eastern subtropics for solution SR (Fig. 5, middle panels), strengthening the stratification considerably there.

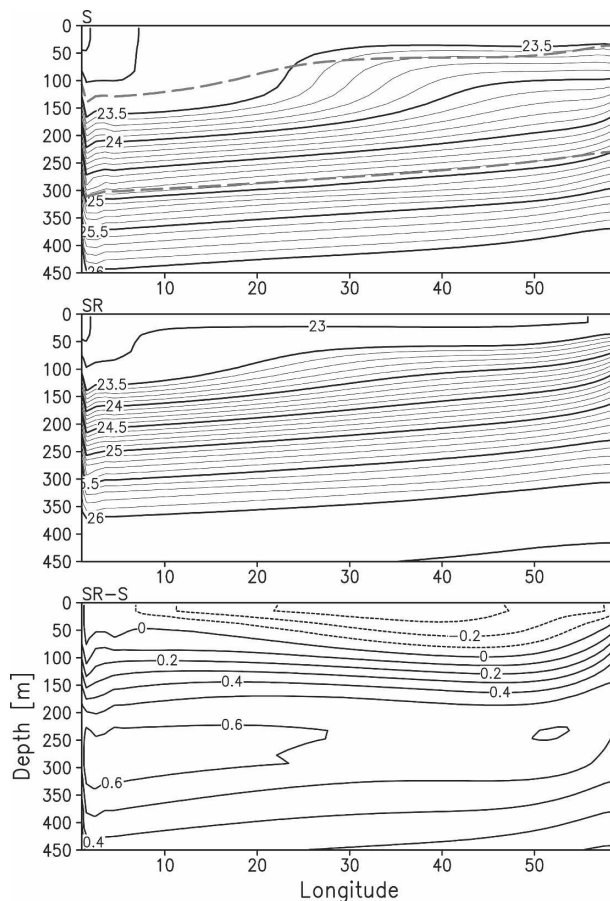


FIG. 5. Longitude–depth section of density fields for (top) solution S, (middle) solution SR, and (bottom) the difference between them, at 21°N in year 40. Contour intervals are 0.1 for the difference and between 23.5 and $26 \sigma_\theta$, and 0.5 elsewhere. In the top panel, contours of 23.5 and $25.5 \sigma_\theta$ for solution SR are also plotted (dashed curves) for easy comparison.

The density difference between the two solutions (Fig. 5, bottom panel) indicates that the signals found in the central to eastern subtropics have a baroclinic structure higher than mode 1. Theoretical studies on the propagation of higher baroclinic Rossby waves (Rhines 1986; McCreary et al. 1992; Liu 1999; Kubokawa and Nagakura 2002) indicate that such signals are primarily advected by the mean circulation, and so spreads southwestward in the direction of the thermocline water circulation. To demonstrate that this is the case for our solutions, Fig. 6 is a plot of the temporal development of the difference in the thickness of the upper thermocline for each solution (h_{up}), where h_{up} is defined by the vertical distance between the 24.5 – and $23.5 \sigma_\theta$ surfaces. To illustrate the subsurface circulation, streamlines on the $24.5 \sigma_\theta$ surface from solution S are included in the lower-right panel (thin contours). Negative Δh_{up} values appear in the central to eastern subtropics

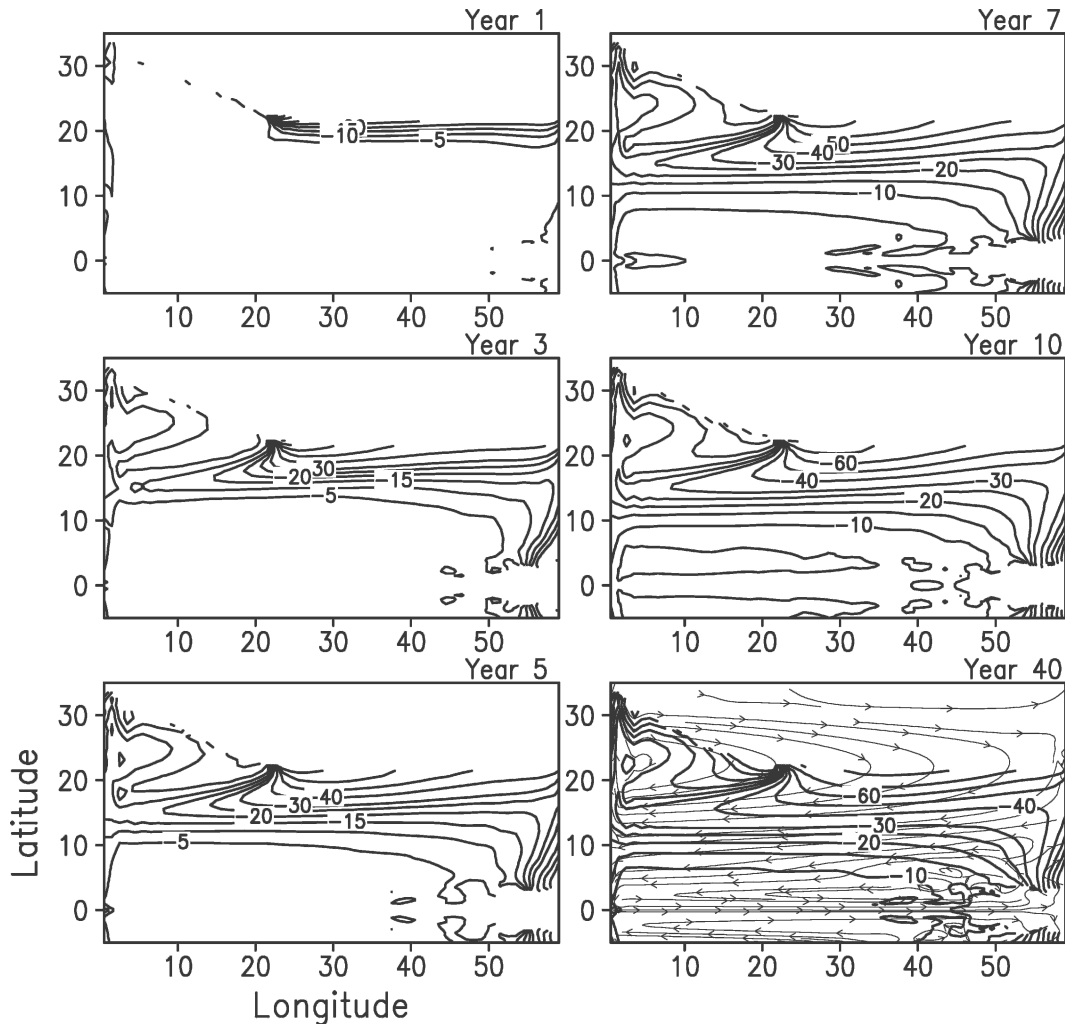


FIG. 6. Plan views of difference in layer thickness from 23.5 to $24.5 \sigma_\theta$ between solution SR and S. Year of each plot is given at the upper-right corner of each panel. Thin contours in the panel for year 40 show streamlines on $24.5 \sigma_\theta$ isopycnal surface. There are no difference lines in the northern basin and far-eastern equatorial region in the plots because sea surface density is greater than $23.5 \sigma_\theta$ there (Fig. 4), and hence h_{up} is not defined.

(year-1 and year-3 panels in Fig. 6), where low-PV mode waters with densities of $23.5\text{--}24.5 \sigma_\theta$ subduct in solution S, that is, downstream of the intersections between the MLD front and outcrop lines in this density range (Fig. 4). Their subsequent spreading in a southwestward direction is apparent.

The central part of the tonguelike structure of the signal arrives at the western boundary from $13^\circ\text{--}15^\circ\text{N}$, north of the latitude where the meridional western boundary current bifurcates, as suggested by the streamlines in the lower-right panel. Thus, the major part of the signal extends poleward, recirculating within the subtropical gyre, while only a small part of it in the southeastern part of the tongue extends equatorward in the western boundary, consistent with the pri-

marily mode-1 structure of the equatorial response (Fig. 3).

3) EKMAN PUMPING

The weakened Ekman pumping in solution SR also directly thins the midlatitude thermocline, as indicated by the rise of the $25.5 \sigma_\theta$ isopycnal in Fig. 5 (top panel, dashed curve). In Fig. 7 the time development of the depth difference of the $25.0 \sigma_\theta$ isopycnal between the two solutions, Δh_{low} , is plotted. This isopycnal lies below the mode waters, and hence provides a better measure of the direct dynamical adjustment to the anomalous Ekman pumping. In each panel, there is a region of shallow Δh_{low} centered near 22°N that extends across the basin, and there is little indication of the southwest-

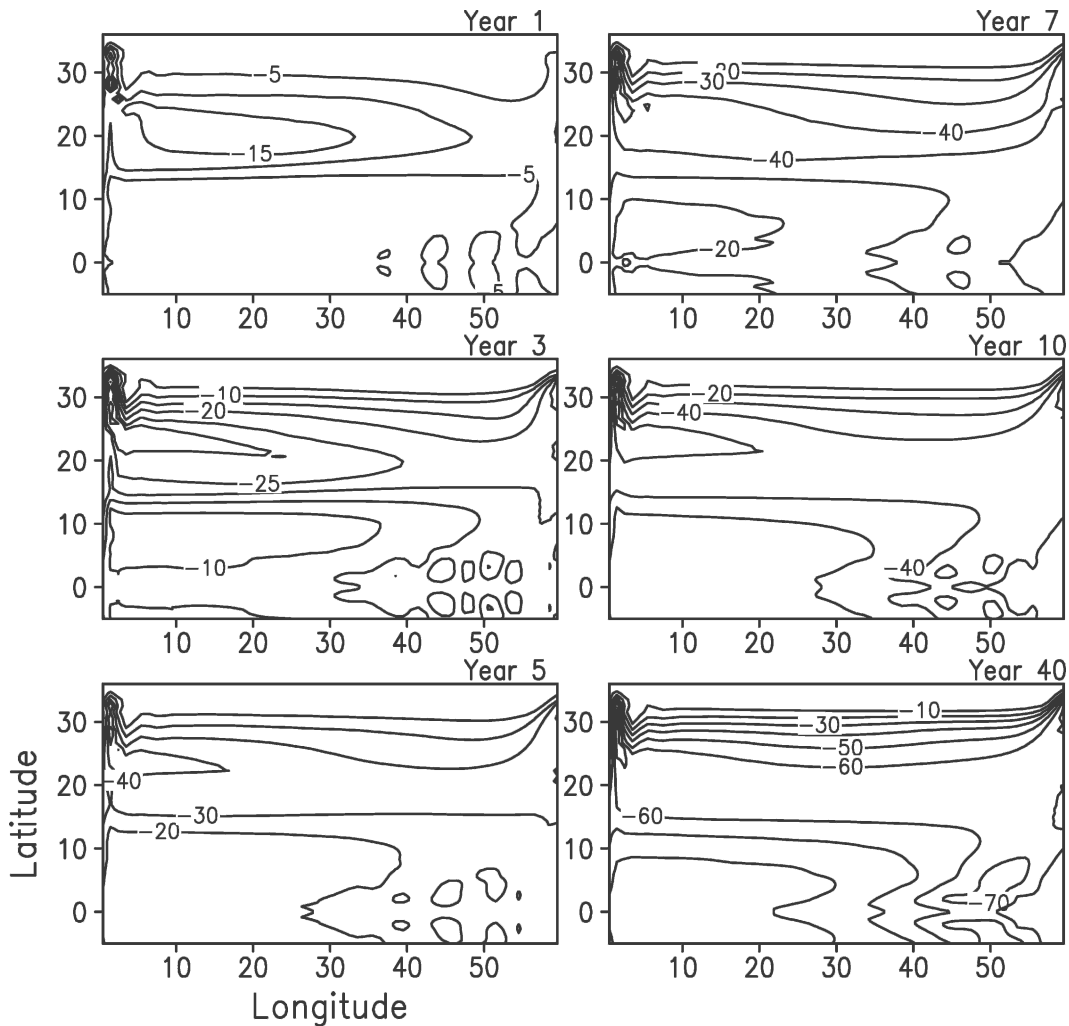


FIG. 7. Plan views of difference in $25.0 \sigma_{\theta}$ isopycnal depth between solutions SR and S. Year of each plot is given at the upper-right corner of each panel. The unit of contour intervals is meters.

ward recirculation evident at shallower levels (Fig. 6). According to theory, the $n = 1$ response spins up most rapidly in response to Ekman pumping, and $n = 1$ Rossby waves are generated that propagate directly westward to the western boundary; higher-order ($n > 1$) Rossby waves are also generated and they propagate along the advective pathway apparent in Fig. 6. The property that Δh_{low} extends only westward indicates that it is almost entirely associated with $n = 1$ signals.

It is well known that effects of this midlatitude response are propagated to the equator along the western boundary by coastal Kelvin and short-wavelength Rossby waves (e.g., Lysne et al. 1997). The western boundary signal then spreads eastward along the equator, poleward along the eastern boundary, and westward from the eastern boundary via equatorial Kelvin, coastal Kelvin, and reflected Rossby waves, respec-

tively, eventually altering the background stratification throughout the basin. Indications of these processes in Fig. 7 are the southward bending of Δh_{low} contours along the western boundary south of about 15°N and the gradual decrease in Δh_{low} throughout the basin. [See Johnson and Marshall (2002, 2004) and Boccaletti (2005) for recent discussions of these, and other, transient processes in a $1\frac{1}{2}$ -layer model and a GCM, respectively.]

A puzzling aspect of this response is that the weakened westerlies should lead to an increase in background Δh_{low} , as water that was piled up within the subtropical gyre in solution S is released to spread throughout the basin in solution SR [see section 4a(1)]. Note that there is a jump in Δh_{low} in the northeastern corner of the basin where eastern boundary signals encounter the sponge layer near the northern boundary,

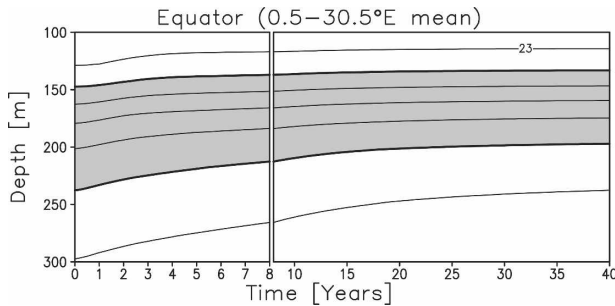


FIG. 8. As in the top panel of Fig. 3, but for solution LR.

an obvious indication of the impact of the sponge layer on the solution. As we shall see, the sponge layer distorts the midlatitude signal that propagates into the Tropics so much that it *reverses* the sign of background Δh_{low} [section 4a(2)].

b. Large basin

To explore the influence of the sponge layer, we obtained solutions in the large basin ($y_n = 60^\circ\text{N}$). In this basin $\tau^x(y_n)$ is unchanged in the sponge layer for the two forcings, eliminating a large part of the direct interaction between the sponge layer and the winds. The mixed layer processes described in section 3a(2) are essentially unchanged in the large-basin solutions. Figure 8, analogous to Fig. 3 for solution SR, illustrates the time development of the equatorial thermocline for solution LR, and the equatorial thermocline also thins much as it did in the small basin.

The similarity of Figs. 3 and 8, with isopycnals rising monotonically in time and deeper isopycnals rising more than shallower ones, suggests that the equatorial thinning in both basins has the same dynamical cause. As discussed below, however, the reason for the thinning in the large basin is different completely, namely, weakened entrainment in the subpolar gyre [section 4b(2)]. Anticipating this result, Fig. 9 is a plot of density sections along 45°N for solutions L (top) and LR (bottom). Isopycnals tilt upward much more gradually in solution LR, a consequence of the weaker Ekman suction there. Area integrals of w at a depth of 50 m over the subpolar region excluding the sponge layer region give upwelling transports of 5.2 and 1.9 Sv ($\text{Sv} \equiv 10^6 \text{ m}^3 \text{ s}^{-1}$) for the two solutions, respectively, confirming that entrainment is weaker in solution LR.

4. Solutions to the 1½-layer model

In section 3, we have shown that the equatorial thermocline in the GCM solutions thins in response to weakened midlatitude westerlies, primarily by means of

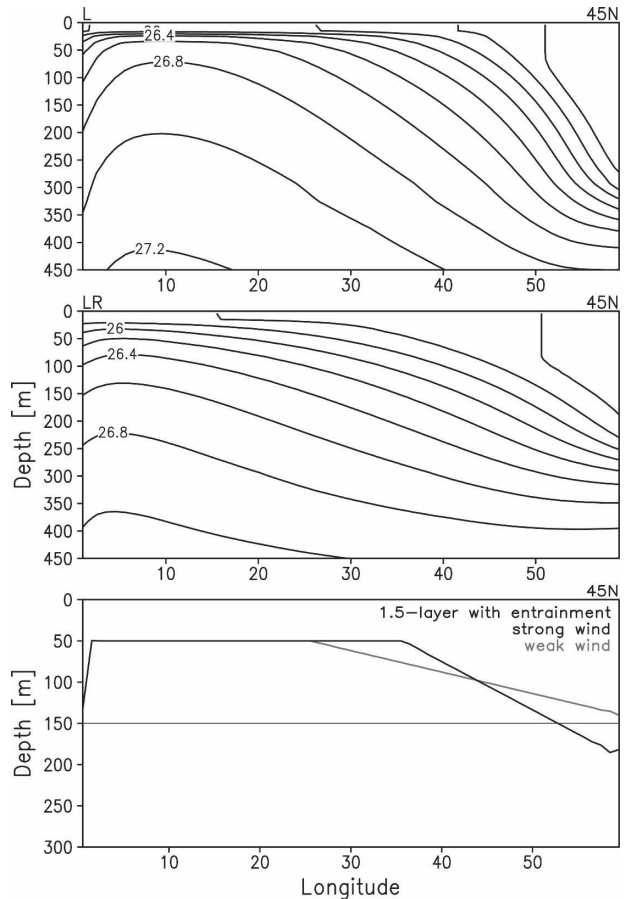


FIG. 9. Longitude–depth section of density fields for solutions (top) L and (middle) LR at 45°N in year 40. (bottom) The h profiles along 45°N from the 1½-layer solutions forced by strong (black) and weak (gray) westerlies. Contour intervals are 0.2 for the density fields.

$n = 1$ signals propagating from midlatitudes. Here, we use the 1½-layer model to investigate the generation of these signals in detail. We find that the causes of equatorial thinning are different in the small and large basins, being traceable to the sponge layer in the former and to entrainment in the subpolar ocean in the latter. [Readers may find it useful to contrast our large-basin solutions with those of Huang (1986) and Huang and Flierl (1987). Their 1½-layer model is similar to ours, except that it does not allow for diapycnal processes; that is, $w_1 = w_s = 0$.]

a. Small basin

To illustrate the significant role of the sponge layer, we contrast solutions both with and without the sponge layer. Since the small basin lacks a subpolar ocean where Ekman suction is strong and entrainment is active, we set $w_s = 0$ for all the solutions discussed in this subsection.

1) NO SPONGE LAYER

Since forcing (9) is x independent and $w_s = 0$, the solution to (6) for h is

$$\begin{aligned}
 h - h_e &= -\frac{f^2}{\beta g' H} w_{ek}(L - x) \\
 &= \frac{1}{\rho_1 g' H} [(y\tau^x)_y - 2\tau^x](L - x), \quad (10)
 \end{aligned}$$

where $w_{ek} = -(\tau^x/\rho_1 f)_y$ is the Ekman pumping velocity, and h_e is the value of h along the eastern boundary to be determined next. For our purposes, equatorial h is the variable of interest, as it corresponds to the depth and stratification of the equatorial thermocline in the GCM solutions. Since $\tau^x(0) = \tau_o$ and $\tau^x_y(0) = 0$, (10) implies that h along the equator is

$$h(x, 0) = h_e - \frac{\tau_o}{\rho_1 g' H} (L - x). \quad (11)$$

Thus, remote forcing by the $\Delta\tau$ part of (9) affects $h(x, 0)$ only through its influence on h_e . Our discussion, then, is focused on understanding the processes that determine h_e .

Integrating (10) over the area of the basin yields a layer volume of

$$\begin{aligned}
 V &= \int_0^L \int_0^{y_n} h \, dx \, dy \\
 &= \frac{1}{2} \frac{L^2}{\rho_1 g' H} y_n \tau^x(y_n) - \frac{L^2}{\rho_1 g' H} \int_0^{y_n} \tau^x \, dy + h_e y_n L. \quad (12)
 \end{aligned}$$

Since there are no sources or sinks of water for the solution considered in this subsection (i.e., $w_1 = w_s = 0$), V must equal the initial layer volume $H y_n L$. With this constraint, (12) yields

$$h_e = H - \frac{1}{2} \frac{L}{\rho_1 g' H} \tau^x(y_n) + \frac{L}{\rho_1 g' H} \frac{1}{y_n} \int_0^{y_n} \tau^x \, dy, \quad (13)$$

which for wind stress (9) and in the small basin (with $y_n = 36^\circ\text{N}$) simplifies to

$$h_e = H + \frac{L}{\rho_1 g' H} \left(\frac{1}{2} \tau_o - \frac{1}{6} \Delta\tau \right). \quad (14)$$

Since $\tau_o < 0$ and > 0 , h_e thins for both the strong and weak winds.

In Fig. 10 h profiles are plotted at $x = 2.5^\circ$ (a location just outside the WBC) from the numerical solutions to (1) forced by strong (solid black curve) and weak (solid gray curve) winds. The profiles confirm solution (10),

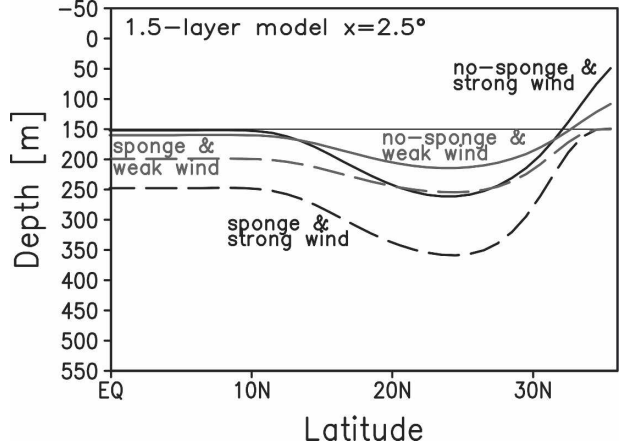


FIG. 10. Plots of steady-state h profiles at $x = 2.5^\circ$ from numerical solutions to the $1\frac{1}{2}$ -layer model in year 40 in the smaller basin, showing responses forced by stronger (black) and weaker (gray) winds without (solid) and with (dotted) sponge layer (4).

for example, with h thickening from the equator to 24°N , the latitude where $\tau^x_{yy} = 0$, and thinning farther to the north. Moreover, equatorial h is thicker in the weak-wind solution by 7.8 m, consistent with the change in h_e predicted by (14), $\Delta h_e = 9.2$ m. Expressed in physical terms, the reason that $\Delta h_e > 0$ is that less mass piles up in the subtropical gyre in the weak-wind solution and the extra mass spreads around the basin to thicken h_e and equatorial h ; the reason Δh_e is so small is that h thickens north of about 31°N , partially compensating for its thinning elsewhere. It is noteworthy that the depth of the equatorial thermocline *thins* from solution S to solution SR (Fig. 2), opposite to the sign of Δh_e for the $1\frac{1}{2}$ -layer solutions. This marked difference in behavior suggests that the thinning in the GCM cannot be explained by wind forcing alone.

2) SPONGE LAYER

When the sponge layer (4) is present along the northern boundary, h is still given by (10) everywhere except at the northern boundary. Just outside the northern boundary layer h is given by

$$h(x, y_n^-) = h_e - \frac{1}{\rho_1 g' H} \tau^x(y_n)(L - x), \quad (15)$$

where $y_n^- = y_n - \epsilon$, $\epsilon \ll y_n$, whereas along the northern boundary the sponge layer requires that $h(x, y_n) = H$. Therefore, there is *necessarily* a geostrophic northern boundary current (NBC) with a transport given by

$$U_{nb}(x) = -\frac{g'H}{f_n} \left[H - h_e + \frac{\tau^x(y_n)}{\rho_1 g' H} (L - x) \right]. \quad (16)$$

Because $\tau^x(y_n) = \tau_o + \Delta\tau > 0$ for both strong and weak winds, U_{nb} accelerates from west to east so that there is a zonally uniform divergence in the NBC, and this divergence is compensated for by uniform entrainment all along the boundary.

Since all exchange with the deep ocean is restricted to the sponge layer by (6), h_e must adjust to also allow *detrainment* within the sponge layer in order to balance the entrainment there. Because coastal Kelvin waves propagate northward along the eastern boundary, there are no wave adjustments that can channel the NBC transport at the northeastern corner back into the interior ocean. Thus, there must be detrainment there to provide a sink for the NBC transport that exactly balances the total upwelling elsewhere in the sponge layer. For the balance, $U_{nb}(x)$ needs to be zero at the western boundary, and the corresponding choice for h_e is

$$h_e = H + \frac{L}{\rho_1 g' H} \tau^x(y_n) = H + \frac{L}{\rho_1 g' H} (\tau_o + \Delta\tau). \quad (17)$$

Any other choice for h_e results in a nonzero NBC in the *northwest* corner, which can be channeled south along the western boundary by coastal Kelvin waves, eventually to spread throughout the basin; in this case h_e will continue to adjust until $U_{nb}(0) = 0$ and it is given by (17). A comparison of (14) and (17) illustrates the significant influence of the sponge layer on h_e , with $h_e - H$ being positive with the sponge layer and negative without it.

In Fig. 10 h profiles are also plotted from the numerical solutions to (6) when there is a sponge layer (dashed curves), and they confirm the analytic results. For example, note that the solutions are uniformly shifted from their counterparts without the sponge layer by 95.9 and 39.2 m for strong and weak forcing, respectively, consistent with the difference in h_e between (14) and (17). More important for our purposes, equatorial h in the weak-wind solution is thinner than it is in the strong-wind solution by 48.9 m, consistent with the predictions of (17), for which $\Delta h_e = -55.0$ m, and opposite to the change without the sponge layer. This property suggests that the cause of the thinning of the equatorial thermocline in solution SR is the GCM's sponge layer.

A distinctive property of the analytic solution is the "cell" within the sponge layer itself, in which there is upwelling spread uniformly along the northern boundary and a compensating downwelling confined to the northeast corner. A similar cell exists in the solutions to both numerical models. In the GCM solution, there is an eastward flow in the upper layer, downwelling at the

northeast corner that attains its maximum amplitude between 200 and 600 m and gradually decreases with depth, and a compensating subsurface westward flow from 400–1000 m to the bottom. At the northeast corner, the boundary transports are 4.6, 6.0, and 8.0 Sv in the analytical and numerical solutions to the 1/2-layer model and the GCM solution, respectively. The reason that the upwelling transport in the GCM is double that in the analytical 1/2-layer solutions is not clear, but is likely traceable to the greater dynamical complexity of the GCM's sponge layer. Nevertheless, the existence of this cell in the GCM solution is strong support that the 1/2-layer model properly represents the basin-scale adjustment processes at work in the GCM.

b. Large basin

Solutions in the large basin differ markedly from those in the small one because of the strong Ekman suction in the subpolar ocean that lifts the thermocline and, if sufficiently strong, drives entrainment of subsurface water into the surface layer. To isolate the effects of entrainment, we contrast solutions with and without this process.

1) NO ENTRAINMENT

Without a sponge layer and entrainment, the solution is also (10) with h_e determined by (13), which in this case yields

$$h_e = H + \frac{L}{\rho_1 g' H} \left(\frac{1}{2} \tau_o + \frac{2}{5} \Delta\tau \right). \quad (18)$$

Note that the sign of the contribution due to $\Delta\tau$ is opposite to that in (14) for the small basin. In Fig. 11 (solid curves) h profiles are plotted for the solutions forced by strong (black curve) and weak (gray curve) winds, and the reason for the change in sign is apparent: In the larger basin, the y integral in (13) is dominated by the large, positive contribution north of 32°N. A consequence of (18) is that equatorial h is thinner for weaker $\Delta\tau$, rather than thicker as in the small basin. The thinning is only -20.8 m, much weaker than it is when entrainment is included (see below).

When there is a sponge layer, the NBC is given by (16) with

$$h_e = H + \frac{L}{\rho_1 g' H} \tau^x(y_n) = H + \frac{L}{\rho_1 g' H} \tau_o, \quad (19)$$

which ensures that $U_{nb}(0) = 0$. Interestingly, there is *no change* in h_e when $\Delta\tau$ is changed. This property is evident from a comparison of the numerical solutions in

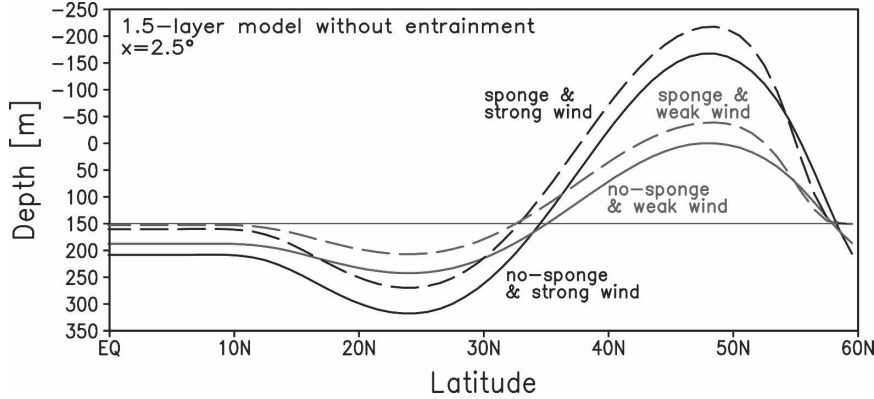


FIG. 11. Plots of steady-state h profiles at $x = 2.5^\circ$ from numerical solutions to the $1\frac{1}{2}$ -layer model in year 40 in the larger basin, showing responses without entrainment forced by stronger (black) and weaker (gray) winds without (solid) and with (dotted) sponge layer (4).

Fig. 11 (dashed curves) in which h profiles for the solutions forced by strong (black) and weak (gray) winds converge to the same equatorial value. The convergence is in marked contrast to the GCM response for which the equatorial thermocline is considerably thinner in solution LR than in solution L (Fig. 8). This model difference indicates that in the large basin the sponge layer is *not the cause* of the thinning.

2) ENTRAINMENT

Without a sponge layer, the response with entrainment is again (10) but with h_e set to different values depending on whether $\Delta\tau$ is strong enough for (7) to apply. Let $\Delta\tau'$ be the critical value of $\Delta\tau$. If $\Delta\tau > \Delta\tau'$, Ekman suction in the subpolar ocean thins h during the spinup until (7) becomes active in some region, in which case h is thereafter fixed to H' and water from

the deep ocean begins to entrain there. Entrainment continues throughout the adjustment until the *minimum* value of h is equal to H' , a constraint that determines h_e .

According to (10), minimum h occurs at the western boundary at the latitude where τ_{yy}^x vanishes in the subpolar ocean ($y = 4y_1$); that is,

$$h_{\min} = h_e - \frac{L}{\rho_1 g' H} \left[\tau_o + \left(\pi + \frac{1}{2} \right) \Delta\tau \right]. \quad (20)$$

When entrainment is active, then, h_e is defined by (20) with $h_{\min} = H'$. The critical wind stress $\Delta\tau'$ is also determined by (20) with $h_{\min} = H'$ and h_e given by (18), yielding

$$\Delta\tau' = \frac{2\rho_1 g' H(H - H') - L\tau_o}{2L(\pi + 1/10)}. \quad (21)$$

Summarizing these results, we have

$$h_e = H + \frac{L}{\rho_1 g' H} \begin{cases} \frac{1}{2} \tau_o + \frac{2}{5} \Delta\tau, & \Delta\tau \leq \Delta\tau' \\ \frac{1}{2} \tau_o + \frac{2}{5} \Delta\tau' + \left(\pi + \frac{1}{2} \right) (\Delta\tau - \Delta\tau'), & \Delta\tau > \Delta\tau' \end{cases}. \quad (22)$$

In this case, h_e changes with $\Delta\tau$ when entrainment is active, resulting in a much thicker value of equatorial h .

In Fig. 12 h profiles from the numerical model are plotted at $x = 2.5^\circ$ for both strong (solid black) and weak (solid gray) winds. Because solutions take so long to adjust to equilibrium when there is entrainment, they are shown at year 250 rather than year 40. (At year 40, they have essentially the same structure as in Fig. 12, but they still have entrainment regions and outside of the regions are uniformly thinner by 110 and 25 m for

strong and weak wind solutions, respectively.) Consistent with the analytic solution, the minimum values of h for both solutions are close to $H' = 50$ m, and they, in fact, attain that value a bit closer to the western boundary. Note that the curves are much deeper than their counterparts without entrainment in Fig. 11. In addition, the thinning of h_e from the strong- to the weak-wind solutions is -189.5 m, in agreement with the change of h_e ($\Delta h_e = -200.3$ m) predicted by (22).

When there is a sponge layer, response (10) is valid

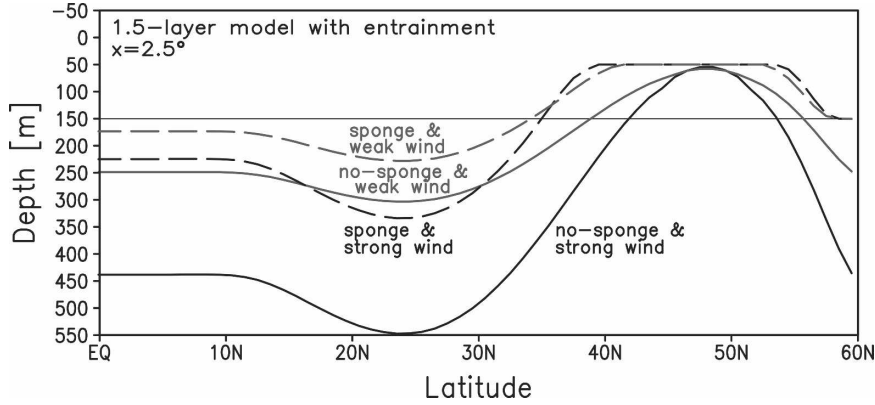


FIG. 12. Plots of steady-state h profiles at $x = 2.5^\circ$ from numerical solutions to the $1\frac{1}{2}$ -layer model in year 250 in the larger basin, showing responses with entrainment forced by stronger (black) and weaker (gray) winds without (solid) and with (dotted) sponge layer (4).

only for $\Delta\tau$ smaller than a critical value $\Delta\tau''$, in which case h_e and h_{\min} are given by (19) and (20). Setting $h_{\min} = H'$ in (20) and with h_e given by (19), it follows that

$$\Delta\tau'' = \frac{\rho_1 g' H H - H'}{L \pi + 1/2}, \quad (23)$$

a somewhat smaller value than $\Delta\tau'$.

When $\Delta\tau > \Delta\tau''$, there must be entrainment in the subpolar ocean. The interior response is then (10) except that $h = H'$ in a region where it would otherwise be less than H' . The region is bounded by the western boundary and the curve, $x_c(y)$, defined by the relation

$$H' - h_e = \frac{f^2}{\beta \rho_1 g' H} w_{ek}[x_c(y) - L], \quad (24)$$

which is obtained by setting $h = H'$ in (10). The latitudes, y_1' and y_2' , where $x_c(y)$ intersects the western boundary are determined from (24) by setting $x_c = 0$, defining them as functions of h_e .

It follows from (6) that the upwelling velocity w_1 in the region where $h = H'$ ($x < x_c$) is w_{ek} . The resulting upwelling transport throughout the basin is

$$\begin{aligned} \varepsilon &= \int_{y_1'}^{y_2'} \int_0^{x_c(y)} w_{ek} dx dy = \int_{y_1'}^{y_2'} x_c(y) w_{ek} dy \\ &= \int_{y_1'}^{y_2'} [x_c(y) - L] w_{ek} dy + L \int_{y_1'}^{y_2'} w_{ek} dy \\ &= \left[-g'H(H' - h_e) \frac{1}{f} - L \frac{\tau^x}{\rho_1 f} \right]_{y_1'}^{y_2'}. \end{aligned} \quad (25)$$

With the sponge layer, there is an NBC with transport (16), and in this case h_e must be adjusted so that all the water entrained in the subpolar gyre is transported northward via the western boundary layer and enters

the sponge layer where it can be detrained. It follows that $U_{nb}(0) = \varepsilon$, yielding the constraint

$$-\frac{g'H}{f_n} \left(H - h_e + \frac{L}{\rho_1 g' H} \tau_0 \right) = \varepsilon. \quad (26)$$

Since y_1' and y_2' are functions of h_e , (25) and (26) provide two equations in the two unknowns, h_e and ε , which can be solved numerically.

In summary, h_e is given by

$$h_e = H + \frac{L}{\rho_1 g' H} \begin{cases} \tau_0, & \Delta\tau \leq \Delta\tau'' \\ \tau_0 + \frac{\rho_1 f_n}{L} \varepsilon, & \Delta\tau > \Delta\tau''. \end{cases} \quad (27)$$

The inequality $\Delta\tau > \Delta\tau''$ is satisfied for both wind fields that force our solutions. Values of $h_e - H$ for the strong and weak winds are 38.5 and -15.3 m, respectively, so that h_e is thinner with weak winds by 53.8 m.

In Fig. 12 solutions to (1) are plotted for the two winds fields when there is entrainment, and they confirm the equatorial thinning predicted by the analytic model. Note, though, that the thinning is considerably less than it is without the sponge layer, a consequence of the thickening due to entrainment being countered by thinning due to detrainment in the sponge layer. Based on these results, we conclude that the thinning of the equatorial thermocline in solution LR is caused by weaker Ekman suction in the subpolar ocean.

With entrainment, the sponge-layer circulation described at the end of section 4a(2) is altered considerably, in this case extending into the interior ocean. It consists of a westward surface flow from the entraining region to the western boundary, northward flow in the WBC into the sponge layer, an eastward NBC, and downwelling all along the northern boundary. Again, a similar circulation is present in the solutions to both

numerical models. In the GCM solution, there is also a compensating, subsurface, westward flow within the sponge layer, which starts from the northeast corner and eventually bends southward at the western boundary.

5. Summary and discussion

In this study, we use an ocean GCM (section 2a) and a 1½-layer model (section 2b) to investigate processes by which changes in the midlatitude winds affect the equatorial stratification. Solutions are forced by idealized winds (9) with strong or weak midlatitude westerlies, and they are found in rectangular basins that extend from the equator to 36°N (small basin) or to 60°N (large basin). In the GCM solutions, the equatorial thermocline shoals and thins when the midlatitude westerlies are reduced in magnitude in both basins (Figs. 3 and 8), and its temporal development suggests that the thinning is mainly caused by $n = 1$ signals. The analyses presented in this paper are all directed toward understanding the causes of these signals.

In the GCM solutions forced by weaker winds (both solutions SR and LR), the most prominent response is the thinning of the subtropical mixed layer (Fig. 4), a consequence of reduced convective mixing due to weaker southward Ekman drift and northward geostrophic flow in the subtropical WBC. As a result, there is less subduction of low-potential-vorticity mode water, and the upper thermocline becomes more strongly stratified in the central to eastern subtropics (Fig. 5). Almost all of this signal, however, recirculates within the subtropical gyre (Fig. 6), and has almost no impact on the equatorial thermocline.

The midlatitude thermocline also responds directly to weakened Ekman pumping, shoaling (deepening) in the subtropical (subpolar) ocean, primarily as an $n = 1$ mode (Figs. 5 and 9). This signal propagates to the western boundary of the basin via Rossby waves and is carried equatorward via coastal Kelvin and short-wavelength Rossby waves. There, it is spread along the equator, leading to a thickening (thinning) of the upper layer there in the small (large) basin in the 1½-layer model without the sponge layer. The property that the equatorial thermocline does not thicken (solution SR) clearly indicates that the thinning is determined by some process other than the wind change itself.

Solutions to the analytic version of the 1½-layer model without entrainment are all given by the Sverdrup-balanced response, differing only in their values of h_e and hence, according to (11), equatorial h . Without a sponge layer, h_e is determined by mass conservation, which requires that the final layer volume is equal

to its initial volume HLy_n , yielding (14) and (18) in the small and large basins, respectively. With a sponge layer, there is necessarily a northern boundary current $U_{nb}(x)$, and h_e is determined by the requirement that $U_{nb}(0) = 0$, yielding (17) and (19). With entrainment, no sponge layer, and for sufficiently strong winds ($\Delta\tau > \Delta\tau'$) water will entrain into the layer until the minimum value of $h = H'$, setting h_e according to (22). With entrainment, a sponge layer, and for sufficiently strong winds ($\Delta\tau > \Delta\tau''$) h is given by the Sverdrup-balanced response only east of curve (24) and $h = H'$ west of it. In this case, h_e is set so that the net entrainment in the subpolar ocean ε is balanced by detrainment in the sponge layer, requiring that $U_{nb}(0) = \varepsilon$ and giving (27). These analytic predictions for h_e (and other properties) are all confirmed in the numerical solutions (Figs. 10, 11, and 12).

The sponge layer generates overturning circulations in the 1½-layer solutions in both the small and large basins. In the small basin, the circulation is an overturning cell confined to the sponge layer, with upwelling spread uniformly along the boundary and a compensating downwelling in the northeast corner of the basin. In the large basin with entrainment, the overturning cell extends to the entraining region of the subpolar ocean. Entrained water flows westward in the interior ocean, northward in a WBC, and within the sponge layer to the northeast corner of the basin. It downwells everywhere in the sponge layer, generating a compensating, subsurface westward current that bends southward at the western boundary eventually to close the cell. Similar sponge-layer circulations are present in our GCM solutions, and likely in other GCM solutions with sponge layers as well.

In the small basin, equatorial h thins in response to weakened westerlies when there is a sponge layer, but it *thickens* when there is not. In the large basin, equatorial h is unaffected by weakened westerlies when there is a sponge layer, but it thins when water is allowed to entrain into the layer in the subpolar gyre. We conclude that the thinning of the equatorial thermocline in the GCM solutions is caused by the sponge layer in the small basin and by weakened entrainment in the subpolar ocean in the large one (Fig. 9).

It is noteworthy that the processes that determine h_e differ fundamentally depending on whether the system includes a sponge layer or entrainment (i.e., allows for diapycnal processes through across-layer transfer by w_1 and w_s). Without either of them, h_e is determined by (11), an area integral over the entire basin, meaning that $|H - h_e|$ will vary depending on the size of the basin. For example, if we include a symmetric, Southern Hemisphere basin, the effect of the changes in the

Northern Hemisphere midlatitude winds on h_e will be *one-half* as great. In contrast, with a sponge layer and/or entrainment h_e is determined independently from the basin area, a more physically appealing result.

One difference between our 1½-layer model and the GCM is that the latter contains explicit thermodynamics, with surface water being heated by the relaxation to T^* . (In our 1½-layer model, heating and cooling is implicit, with water parcels instantly changing their temperature when they entrain into, or detrain from, the active layer.) Thus, the property that the equatorial thermocline is deeper in solution L than in solution LR could result from forcing by tropical heating in the equatorial cold tongue (Boccaletti et al. 2004). To check this idea, we followed the time development of a test run forced by strong winds using solution LR at year 40 (near equilibrium) as its initial state. There was never any anomalous near-equatorial heating throughout the adjustment, but rather cooling (a response to the deepening of the tropical thermocline). The heating needed to warm entrained subpolar water was supplied by extraequatorial, surface fluxes as the entrained water spread equatorward to fill the tropical basin.

The stratification of the equatorial ocean is recognized as being important for ENSO properties (Fedorov and Philander 2000), and it is often specified as an external parameter in intermediate coupled models (e.g., Wang and An 2002). Our results suggest that it may be sensitive to changes in midlatitude winds through their influence on entrainment in the subpolar ocean. Indeed, there are significant changes in the strength and distribution of North Pacific surface winds on decadal-to-interdecadal time scales (Deser et al. 1996; Yasuda and Hanawa 1997; Mantua et al. 1997). Yet, solutions to ocean GCM forced by observed midlatitude winds do not have a major effect on the equatorial thermocline (Hazeleger et al. 2001; Nonaka et al. 2002). One possible reason for this lack of sensitivity is that the observed wind variations are not large enough. Another is that previous modeling studies have focused on forcing by decadal-varying winds. Given the long adjustment times evident in Figs. 3 and 8, one expects the amplitude of the response to an oscillating wind to be considerably weaker than the steady-state difference between solutions L and LR (Klinger et al. 2002). To confirm this idea, we carried out a set of experiments using the 1½-layer model with the sponge layer and entrainment, allowing $\Delta\tau$ to vary sinusoidally from its weak to strong values with periods of 10 and 20 yr, finding that the amplitude of the response is only 1/5 and 1/3, respectively, of the steady-state difference.

Midlatitude wind forcing may have been quite different in the geological past. For example, the equatorial

Pacific is considered to be a key element of climatic feedback that gives rise to a solar-induced glacier–interglacial cycle (Visser et al. 2003). Superimposed on a tropicalwide cooling, some observations (Koutavas et al. 2002; Stott et al. 2002) indicate that the equatorial Pacific was in a permanent El Niño state with a reduced zonal SST gradient during the Last Glacial Maximum (LGM). Simulations with atmospheric GCMs suggest that at that time midlatitude westerly winds over the North Pacific strengthened substantially (e.g., Kitoh and Murakami 2002). According to our results, such a wind change would increase entrainment in the subpolar ocean, deepening the equatorial thermocline and reducing its stratification. Both effects would increase the subsurface temperature that is upwelled/entrained into the equatorial mixed layer, reducing the cooling due to upwelling there. With Bjerknes (1969) feedback active, these extratropical-triggered changes in the equatorial thermocline could lead to a basinwide relaxation of the trade winds and zonal SST gradient.

In conclusion, our results with idealized models suggest that midlatitude wind variability can induce subsurface temperature anomalies on the equator without any change in STC strength or its properties, as is the case in the Kleeman et al. (1999) and Gu and Philander (1997) studies. Rather, it is changes in the strength of entrainment in the subpolar gyre that leads to equatorial temperature anomalies by modifying the amount of upper-layer water throughout the basin. Whether this mechanism is also influential in more realistic models needs to be examined, especially at very long time scales.

Acknowledgments. This study was supported by the Frontier Research Center for Global Change (FRCGC), and by the Japan Agency for Marine–Earth Science and Technology (JAMSTEC) through its sponsorship of the International Pacific Research Center (IPRC). Masami Nonaka was also partly supported by a Grant-in-Aid for Young Scientist (16740277) by the Ministry of Education, Culture, Sports, Science, and Technology (MEXT) of Japan.

REFERENCES

- An, S.-I., and F.-F. Jin, 2000: An eigen-analysis of the interdecadal changes in the structure and frequency of ENSO mode. *Geophys. Res. Lett.*, **27**, 2573–2576.
- Bjerknes, J., 1969: Atmospheric teleconnections from the equatorial Pacific. *Mon. Wea. Rev.*, **97**, 163–172.
- Boccaletti, G., 2005: Timescales and dynamics of the formation of a thermocline. *Dyn. Atmos. Oceans*, **39**, 21–40.
- , R. C. Pacanowski, and S. G. H. Philander, 2004: The thermal structure of the upper ocean. *J. Phys. Oceanogr.*, **34**, 888–902.
- Deser, C., M. A. Alexander, and M. S. Timlin, 1996: Upper-ocean

- thermal variations in the North Pacific during 1970–1991. *J. Climate*, **9**, 1840–1855.
- Fedorov, A. V., and S. G. H. Philander, 2000: Is El Niño changing? *Science*, **288**, 1997–2002.
- Gu, D., and S. G. H. Philander, 1997: Interdecadal climate fluctuations that depend on exchanges between the Tropics and extratropics. *Science*, **275**, 805–807.
- Hazeleger, W., M. Visbeck, M. Cane, A. Karspeck, and N. Naik, 2001: Decadal upper ocean temperature variability in the tropical Pacific. *J. Geophys. Res.*, **106**, 8971–8988.
- Huang, R.-X., 1986: Numerical simulation of wind-driven circulation in a subtropical/subpolar basin. *J. Phys. Oceanogr.*, **16**, 1636–1650.
- , and G. R. Flierl, 1987: Two-layer models of the thermocline and current structure in subtropical/subpolar gyres. *J. Phys. Oceanogr.*, **17**, 872–884.
- Johnson, H. L., and D. P. Marshall, 2002: A theory for the surface Atlantic response to thermocline variability. *J. Phys. Oceanogr.*, **32**, 1121–1132.
- , and —, 2004: Global teleconnections of meridional overturning circulation anomalies. *J. Phys. Oceanogr.*, **34**, 1702–1722.
- Kitoh, A., and S. Murakami, 2002: Tropical Pacific climate at the mid-Holocene and the Last Glacial Maximum simulated by a coupled ocean–atmosphere general circulation model. *Paleoceanography*, **17**, 1047, doi:10.1029/2001PA000724.
- Kleeman, R., J. P. McCreary, and B. A. Klinger, 1999: A mechanism for generating ENSO decadal variability. *Geophys. Res. Lett.*, **26**, 1743–1746.
- Klinger, B. A., J. P. McCreary, and R. Kleeman, 2002: The relationship between oscillating subtropical wind stress and equatorial temperature. *J. Phys. Oceanogr.*, **32**, 1507–1521.
- Koutavas, A., J. Lynch-Stieglitz, T. M. Marchitto, and J. P. Sachs, 2002: El Niño-like pattern in ice age tropical Pacific sea surface temperature. *Science*, **297**, 226–230.
- Kubokawa, A., 1999: Ventilated thermocline strongly affected by a deep mixed layer: A theory for subtropical countercurrent. *J. Phys. Oceanogr.*, **29**, 1314–1333.
- , and M. Nagakura, 2002: Linear planetary wave dynamics in a 2.5-layer ventilated thermocline model. *J. Mar. Res.*, **60**, 367–404.
- Liu, Z., 1999: Forced planetary wave response in a thermocline gyre. *J. Phys. Oceanogr.*, **29**, 1036–1055.
- , and S. G. H. Philander, 1995: How different wind stress patterns affect the tropical–subtropical circulations of the upper ocean. *J. Phys. Oceanogr.*, **25**, 449–462.
- Lysne, J., P. Chang, and B. Giese, 1997: Impact of the extratropical Pacific on equatorial variability. *Geophys. Res. Lett.*, **24**, 2589–2592.
- Mantua, N. J., S. R. Hare, Y. Zhang, J. M. Wallace, and R. C. Francis, 1997: A Pacific interdecadal climate oscillation with impacts on salmon production. *Bull. Amer. Meteor. Soc.*, **78**, 1069–1079.
- McCreary, J. P., and P. Lu, 1994: Interaction between the subtropical and equatorial ocean circulation: The subtropical cell. *J. Phys. Oceanogr.*, **24**, 466–497.
- , Y. Fukamachi, and P. Lu, 1992: A nonlinear mechanism for maintaining coastally trapped eastern boundary currents. *J. Geophys. Res.*, **97**, 5677–5692.
- Nishikawa, S., 2003: A numerical study on the mixed layer front (in Japanese). Master's thesis, Graduate School of Environmental Earth Science, Hokkaido University, Sapporo, Japan, 76 pp.
- Nonaka, M., S.-P. Xie, and J. P. McCreary, 2002: Decadal variations in the subtropical cells and equatorial Pacific SST. *Geophys. Res. Lett.*, **29**, 1117, doi:10.1029/2001GL013676.
- Pacanowski, R. C., and S. G. H. Philander, 1981: Parameterization of vertical mixing in numerical models of tropical oceans. *J. Phys. Oceanogr.*, **11**, 1443–1451.
- , K. W. Dixon, and A. Rosati, 1991: The GFDL Modular Ocean Model Users Guide. GFDL Ocean Group Tech. Rep. 2, 16 pp.
- Pedlosky, J., 1996: *Ocean Circulation Theory*. Springer, 453 pp.
- Qiu, B., and R. X. Huang, 1995: Ventilation of the North Atlantic and North Pacific: Subduction versus obduction. *J. Phys. Oceanogr.*, **25**, 2374–2390.
- Rhines, P. B., 1986: Vorticity dynamics of the ocean general circulation. *Annu. Rev. Fluid Mech.*, **18**, 433–497.
- Solomon, A., J. P. McCreary, R. Kleeman, and B. Klinger, 2003: Interannual and decadal variability in an intermediate coupled model of the Pacific region. *J. Climate*, **16**, 383–405.
- Stott, L., C. Poulsen, S. Lund, and R. Thunell, 2002: Super ENSO and global climate oscillations at millennial time scales. *Science*, **297**, 222–226.
- Visser, K., R. Thunell, and L. Stott, 2003: Magnitude and timing of temperature change in the Indo-Pacific warm pool during deglaciation. *Nature*, **421**, 152–155.
- Wang, B., and S.-I. An, 2002: A mechanism for decadal changes of ENSO behavior: Roles of background wind changes. *Climate Dyn.*, **18**, 475–486.
- Xie, S.-P., T. Kunitani, A. Kubokawa, M. Nonaka, and S. Hosoda, 2000: Interdecadal thermocline variability in the North Pacific for 1958–1997: A GCM simulation. *J. Phys. Oceanogr.*, **30**, 2798–2813.
- Yasuda, T., and K. Hanawa, 1997: Decadal changes in the mode water in the midlatitude North Pacific. *J. Phys. Oceanogr.*, **27**, 858–870.